Supplementary Information (SI) for Physical Chemistry Chemical Physics.

Supporting Information: Machine learning of the architecture-property relationship in graft polymers

Kevin V. Bigting,[†] Jordan Carden,[†] Shubhadeep Nag,[‡] Jimmy Lawrence,[‡] Yen-Fang Su,[¶] and Yaxin An[*,‡]

† *Department of Computer Science and Engineering, Louisiana State University, LA, 70803, United States*

‡*Cain Department of Chemical Engineering, Louisiana State University, LA 70808, United States*

¶*Department of Civil and Environmental Engineering, Louisiana State University, LA 70808, United States*

E-mail: yxan@lsu.edu

S1 Computational Details

S1.1 Model Description

Coarse-grained bead-spring models have been extensively used to study polymer conformations and properties. Previous studies by Karuth *et al.*[1] and Chremos *et al.*[2] successfully employed this model to predict the glass transition temperature and unentangled diffusion behavior of polymers. In this work, we adopt the same model to compute the four key properties of graft polymers: the glass transition temperature (T_g), self-diffusion coefficient (D), radius of gyration (R_g), and density (ρ).

The total potential energy of the system is given by:

$$U(r) = \sum_{i,j} k_{b,ij}(r_{ij} - r_0)^2 + \sum_{i,j,k} k_{\theta,ijk}(1 + \cos\theta_{ijk}) + \sum_{i,j} 4\epsilon\left[\left(\frac{r_{ij}}{\sigma}\right)^{12} - \left(\frac{r_{ij}}{\sigma}\right)^{6}\right] \tag{S.1}$$

where $r_0 = 0.99\sigma$ is the equilibrium bond length, and $k_b = 2500\epsilon/\sigma^2$ is the bond force constant. The chain stiffness is controlled by k_θ, which governs the flexibility of both the backbone and side chains. In this study, we use a fixed $k_\theta = 15\epsilon$. The parameters ϵ and σ denote the depth of the Lennard-Jones (LJ) potential well and the characteristic distance at which the LJ potential is zero, respectively. The cutoff distance for nonbonded interactions is set to $r_c = 2.5\sigma$.

S1.2 Simulation Details

Molecular dynamics simulations were performed using the LAMMPS package.[3] All simulations were conducted in the isothermal-isobaric (NPT) ensemble. Temperature and pressure were controlled using the Nose-Hoover thermostat and barostat, respectively. The equations of motion were integrated using the velocity-Verlet algorithm with a timestep of 0.005τ. Periodic boundary conditions were applied in all three spatial directions.

All simulations were conducted using reduced units, where energy (ϵ), length (σ), and mass (m) are set as fundamental units.[4] The temperature is expressed in reduced form as $T^* = k_B T/\epsilon$, and time is scaled as $\tau^* = \tau(m\sigma^2/\epsilon)^{1/2}$. The self-diffusion coefficient is reported in reduced units of σ^2/τ, and density is given in σ^{-3}. These reduced units ensure generality and allow comparison across different polymer systems. The simulation trajectories were analyzed to compute the target properties as detailed below.

S1.3 Glass Transition Temperature, T_g

The methodology for computing the glass transition temperature follows the approach described in ref.[1] We briefly summarize the procedure here.

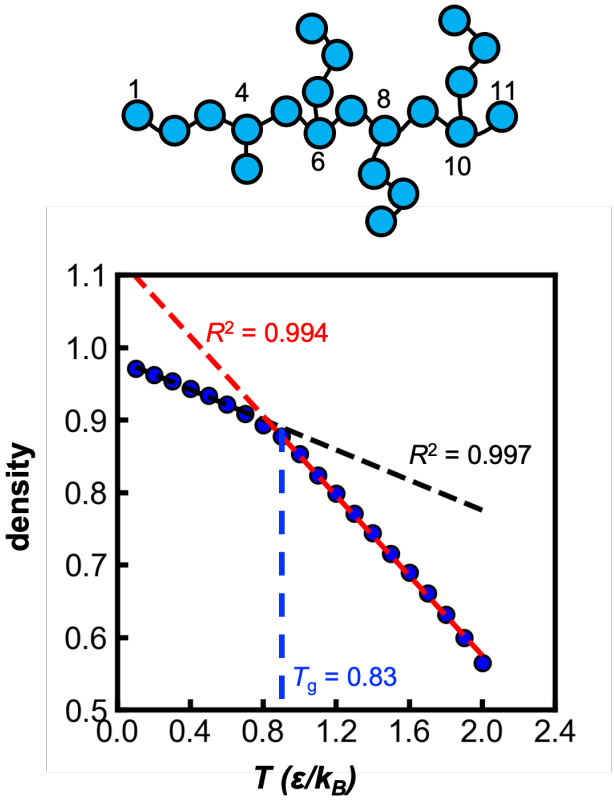

Figure S1: The Density versus temperature for calculation of the T_g of a representative graft polymer is shown here. The black and red dashed lines represent the linear fitting at the low-T and high-T regimes, respectively. The R^2 scores for the linear fitting are as high as 0.997 and 0.994. The T_g is at which these two fitted lines cross, 0.83 ϵ/k_B.

A total of 500 polymers were randomly placed in a cubic simulation box with an initial length of 300σ and subsequently compressed under high pressure to achieve a density in the range of 0.5–1.0, consistent with previous studies.[1] The polymer melt was equilibrated at a high temperature of 2.0 ϵ/k_B and a pressure of 0 in the NPT ensemble before being cooled at a rate of 1.3×10^{-6} ϵ/k_B. NPT simulations were performed across a temperature range of 0.5–2.0 ϵ/k_B in increments of 0.1.

The glass transition temperature was determined by analyzing the density as a function of temperature. The density data were divided into two blocks, each fitted with a linear regression function. To determine the optimal transition point, a brute-force approach was conceptualized and employed by us to optimize the partition maximizing the sum of the R^2 scores from the two regression fits. The temperature at which the two linear regression lines intersect was identified as the glass transition temperature, T_g. A representative figure is provided here to demonstrate the result, as shown below (see Fig. S1).

S1.4 Self-Diffusion Coefficient in the Melt State, D

The self-diffusion coefficient (D) of polymers in the melt state was computed at a reduced temperature of $T = 2.0\epsilon/k_B$ using the mean squared displacement (MSD) and the Einstein relation:

$$D = \lim_{\Delta\tau\to\infty} \frac{1}{6\Delta\tau} \langle |\vec{r}_{t+\Delta\tau} - \vec{r}_t|^2 \rangle, \tag{S.2}$$

where $\vec{r}$ is the position of the center of mass of a tagged polymer chain, and $\langle \cdots \rangle$ denotes an ensemble average. The term $|\vec{r}_{t+\Delta\tau} - \vec{r}_t|^2$ represents the MSD of the polymer's center of mass. The diffusion coefficient was extracted from the linear regime of the MSD curve, which was computed over the last 4 million steps of the MD simulations, ensuring the simulation is long enough to reach the diffusive regime.[5]

S2 Effect of Backbone and Side-Chain Rigidity on Glass Transition Temperature

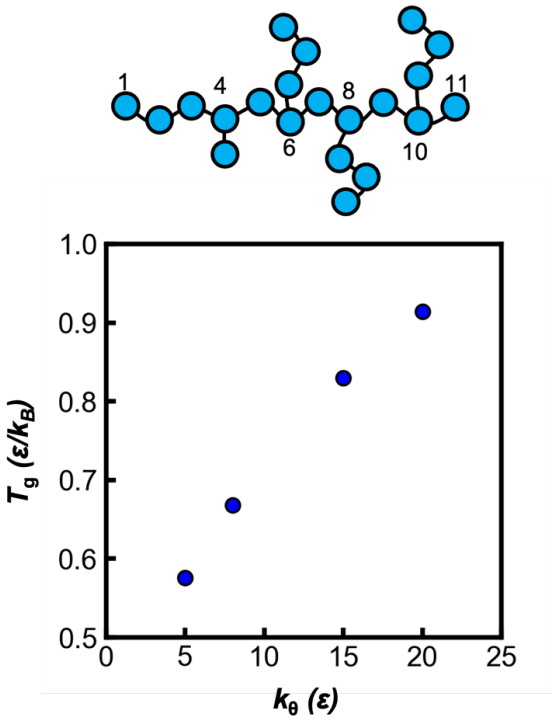

Figure S2: Effect of angular stiffness k_θ on the T_g is shown here for a representative graft polymer (N_{bb} = 11, side chains are attached at backbone beads 4, 6, 8, and 10 with N_{sc} of 1, 3, 3, and 3, respectively).

To assess the influence of polymer rigidity on glass formation, we performed molecular dynamics simulations of a representative graft polymer with parameters N_{bb} =11, N_{sc} =5, and grafting density f =0.45. The rigidity was modulated by varying the angular force constant k_θ, applied identically to both backbone and side-chain segments to represent the flexible–flexible (F–F) and stiff–stiff (S–S) limits.[6]

As shown in Fig. S2, the T_g increases monotonically from 0.576 to 0.914 ϵ/k_B as k_θ increases from 5 to 20 ϵ, indicating enhanced resistance to conformational rearrangement with increasing chain stiffness. This trend is in agreement with theoretical predictions and simulation results from generalized entropy theory studies.[7,8]

S3 Machine learning (ML) models

S3.1 Featurization of graft polymers

Physical descriptors: Each polymer is represented by six physical descriptors as list below:

- the number of beads in the backbone: N_{bb}
- the total number of beads: N_{tot}
- the grafting density: f
- the average number of beads in the side chains: $N_{sc,ave}$
- the maximum number of beads in the side chains: $N_{sc,max}$
- the minimum number of beads in the side chains: $N_{sc,min}$

Graphical descriptors: Each polymer is represented as an undirected graph where beads are nodes, and bonds are edges. We adopted the eleven graphical descriptors from the ref[9]

- Number of nodes: N_{nodes}
- Number of edges: N_{edges}
- Algebraic connectivity: λ_{alg}
- Diameter: ϕ_{diam}
- Radius: ϕ_{rad}
- Average degree: $\bar{d}$
- Average neighbor degree: $\bar{d}_{nb}$
- Network density: δ

- Mean degree centrality: C_{deg}
- Mean betweenness centrality: C_{bet}
- Degree assortativity coefficient: r_{deg}

Spearman's Rank Correlation Coefficient Among the six physical descriptors, four—backbone length (N_{bb}), total number of beads (N_{tot}), average side-chain length ($N_{sc,ave}$), and maximum side-chain length ($N_{sc,max}$)—showed strong correlations (coefficient $\geq$ 0.8 or $\leq$ -0.8) with all target properties, whereas the remaining two exhibited negligible correlations. Among the eleven graphical descriptors, most were strongly correlated with the target properties, except for average neighbor degree ($\bar{d}_{nb}$) and Degree assortativity coefficient (r_{deg}), which showed weak correlation.

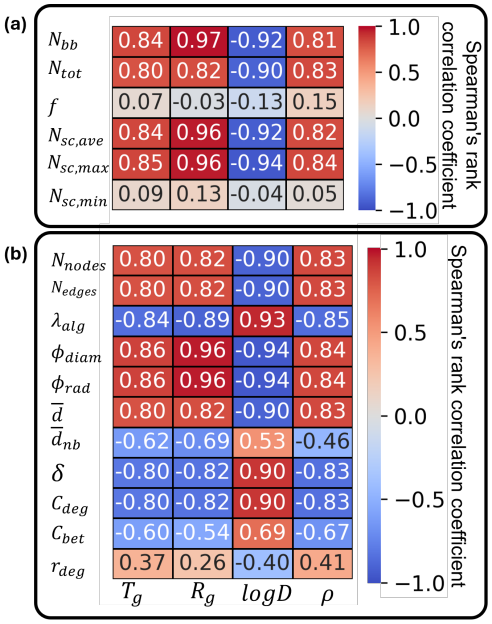

Figure S3: The Spearman's rank correlation coefficients (a) between 6 physical descriptors with four properties and (b) between 11 graphical descriptors with the four properties. Representations of descriptor symbols are defined in Section S2 of SI.

Images

The graft polymer structures were represented as 26×60 pixels grayscale images as input into the convolutional neural network (CNN). The rationale behind choosing such an image is

based directly on the structural characteristics of the polymer dataset. The dataset comprises branched polymers with a maximum backbone length of 60 beads and sidechain lengths of up to 25 beads. To encode this structure, each input image is constructed to explicitly represent these parameters: the first row encodes the presence of backbone beads, while each subsequent row represents sidechain units attached to the corresponding backbone node indexed by column position. Therefore, it follows:

- The first row encodes the presence of backbone beads, where each column index corresponds to a specific backbone position.
- The next 25 rows encode the side-chain units. In these rows, each column reflects the number of side-chain beads attached to the corresponding backbone bead.

Furthermore, pixels in the matrix indicated different types of polymer beads: black pixels (grayscale value = 0) denoted backbone beads, gray pixels (grayscale value = 127) represented sidechain beads, and white pixels (grayscale value = 255) indicated the absence of beads.

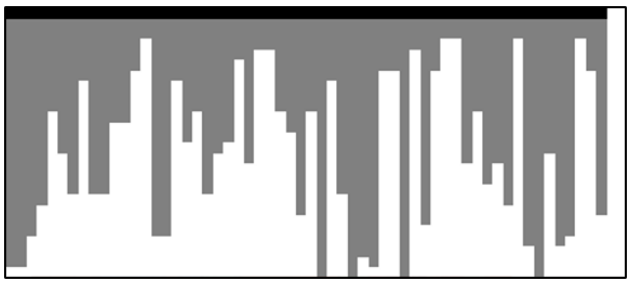

Figure S4: A representative image for a bottlebrush polymer (grafting density $f = 1.0$) with a bakcbone length of 58. The side-chain length varies randomly from 1 to 26. Black pixels represent the backbone, while gray pixels are for the side chains.

S3.2 DNN models

We developed Dense Neural Network (DNN) models using the TensorFlow library, and optimized them through a series of techniques, including feature scaling, output transforma-

tion and normalization, K-fold cross-validation, dropout regularization, learning rate adjustments, and early stopping. The activation function used was ReLU, and the Adam optimizer was employed for gradient descent. Various model configurations were tested to identify the architecture that maximized predictive accuracy. For example, the number of hidden layers and hidden nodes in the first layer are optimized (Figure S6 (a)).

The dataset comprising 500 graft polymer structures was randomly partitioned into training, validation, and test sets with a ratio of 60:20:20. This partitioning ensures a balanced and unbiased evaluation of model performance. A statistical overview of the four target properties, glass transition temperature (T_g), packing density (ρ), radius of gyration (R_g), and diffusion coefficient (D), is provided in Fig. S5. Both T_g and ρ exhibit unimodal distributions, indicating relatively uniform variation across the dataset. In contrast, R_g displays a bimodal distribution, reflecting structural diversity in polymer conformations. The distribution of D is notably skewed toward lower values, suggesting that slower-diffusing polymer configurations are more prevalent in the dataset.

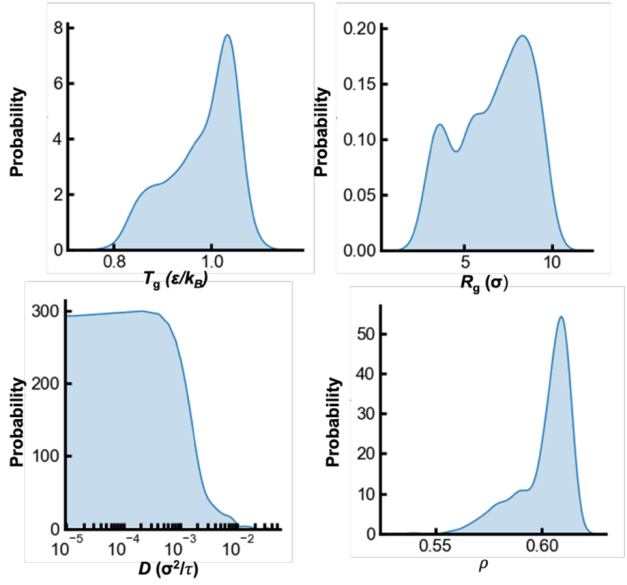

Figure S5: The kernel density estimation of the four properties across all 500 polymers.

The final optimized DNN architecture consisted of four fully connected dense layers with 512 1024, 512, and 32 nodes, respectively, all activated by the ReLU function. A dropout

rate of 40% was applied during training to enhance generalization, with all neurons activated during inference. Input features were scaled using the Min-Max scaler, and the model was trained with a batch size of 64. Model performance was evaluated based on the average R^2 score and root mean squared error (RMSE) across all folds, demonstrating consistent and reliable predictive accuracy.

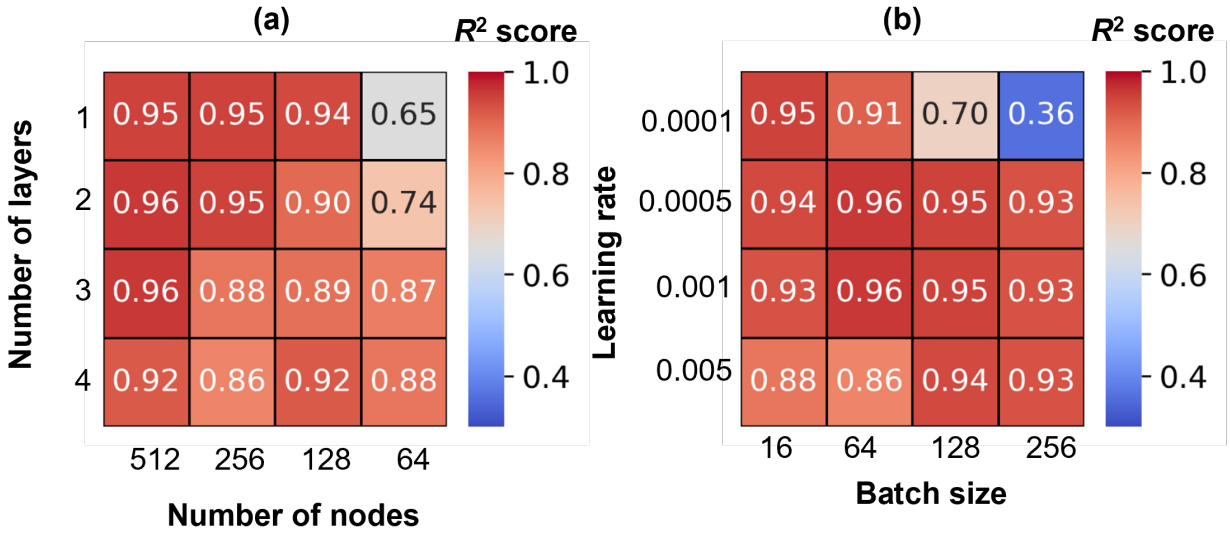

Figure S6: (a) The R^2 scores of the DNN models with different number of hidden layers and hidden nodes (first layer) for predicting the D. (b)The R^2 scores of the CNN models (for predicting D) at different batch sizes and learning rates.

Convergence Behavior

To evaluate the convergence behavior and potential overfitting of the DNN model, we monitored the training and validation loss across epochs for all model architectures considered. In Fig. S7, we plotted the training loss (black) and validation loss (red) curve for DNN. From the figure, we can see that both of these curves steadily decrease and approach minimal values. The convergence behavior confirms that the models are trained in a stable regime and achieve consistent optimization across properties.

Prediction Performance of DNN Models

To evaluate the predictive accuracy of DNN models trained on black-and-white polymer representations, we compare the predicted and true values of T_g, R_g, D, and ρ. Fig. S8

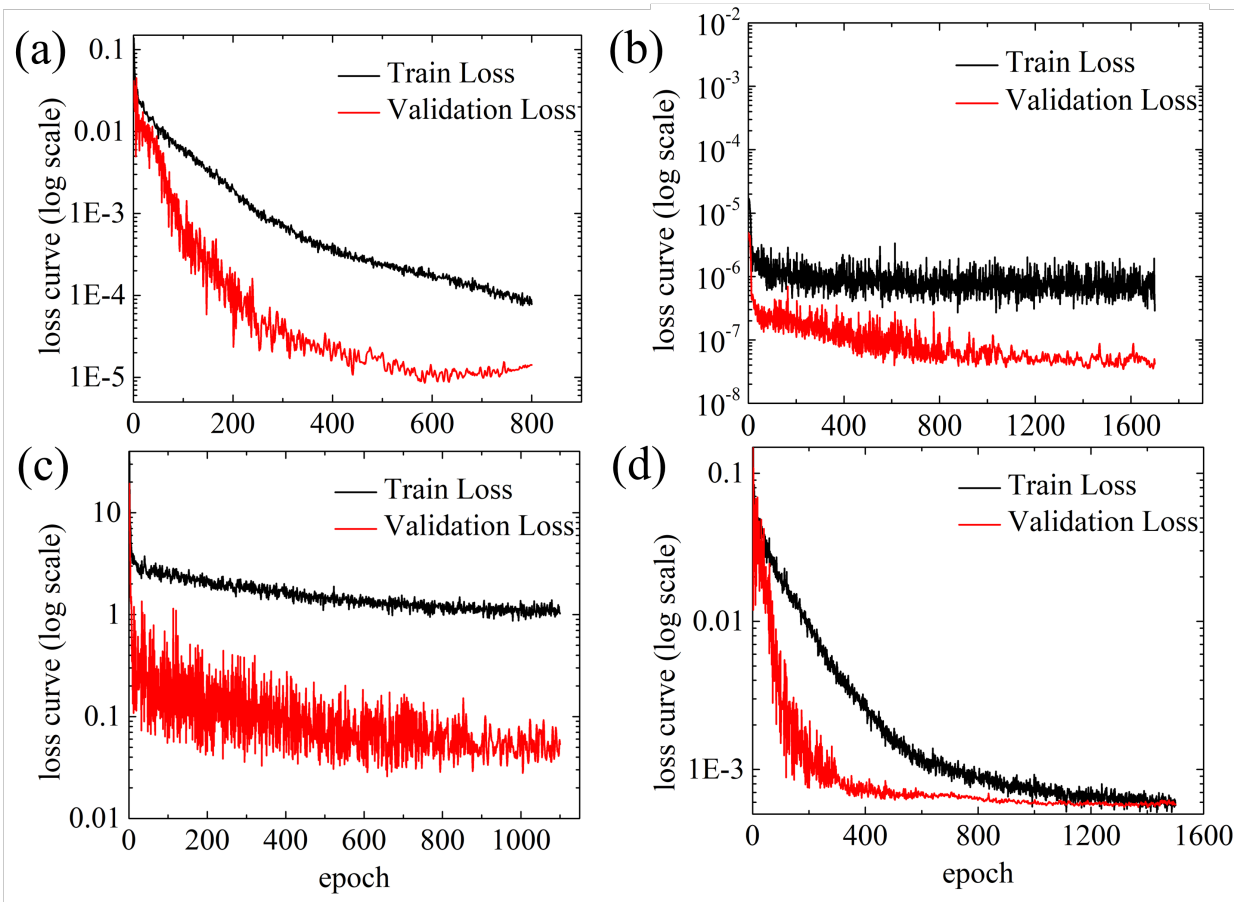

Figure S7: The training and validation loss curves for DNN models predicting (a) density (ρ), (b) diffusivity (D), (c) radius of gyration (R_g), and (d) glass transition temperature (T_g). The main figures show the evolution of loss (in log scale) over a set of training epochs. Black curves represent training loss, and red curves represent validation loss. All models exhibit rapid convergence and stable training behavior, with no signs of significant overfitting.

presents these comparisons, where the red dashed line represents the ideal scenario where predicted values perfectly match MD simulation results.

In Fig. S8(a), we showed how the DNN model accurately predicts T_g, with most data points closely following the diagonal reference line. Despite an R^2 score slightly lower than other properties, the RMSE of 0.025 indicates a relatively small prediction error, confirming the model's reliability within the variability of MD simulations. Similarly, the predicted R_g values (see Fig. S8(b)) exhibit strong agreement with the true values, with an RMSE of 0.34, indicating the DNN model's effectiveness in capturing polymer conformations.

The self-diffusion coefficient, D (see Fig. S8(c)) spans several orders of magnitude, yet the

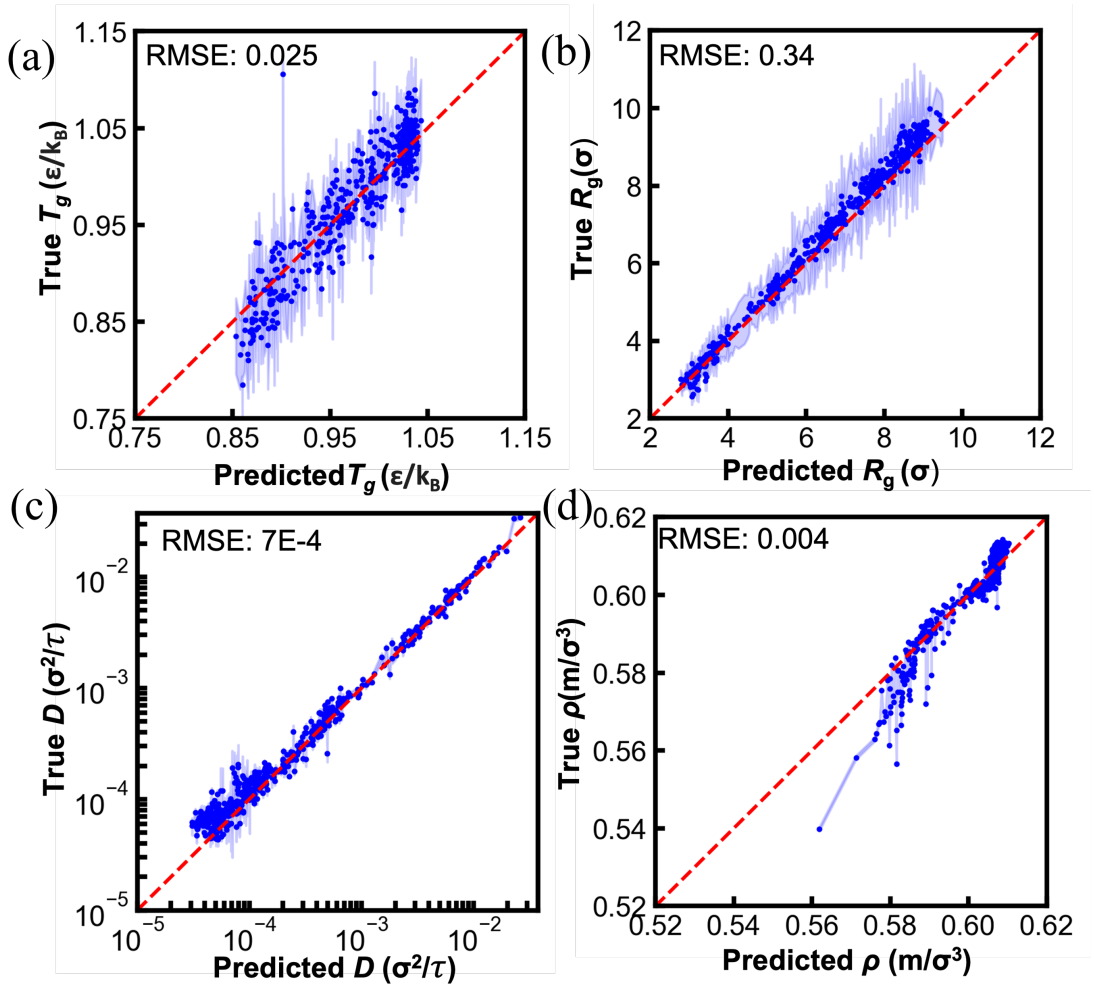

Figure S8: Performance of the DNN models in predicting key properties of graft polymers. Each subplot shows the correlation between predicted and true values for (a) glass transition temperature (T_g), (b) radius of gyration (R_g), (c) self-diffusion coefficient (D), and (d) packing density. The red dashed line represents the ideal perfect prediction ($y = x$), and blue points indicate individual data samples with error bars. The root mean square error (RMSE) for each property is displayed in the respective plots, quantifying the model's predictive accuracy.

DNN model successfully follows the expected trend. The RMSE is only 7×10^{-4}, the data distribution aligns well with the diagonal reference, demonstrating the model's capability in predicting polymer diffusion. Although R^2 score of the DNN model is slightly small, 0.88 in predicting ρ (Fig. S8(d)), it achieves an RMSE of 0.004, comparable to the standard deviation of MD simulation results. The predicted values exhibit minimal deviation from the true values, highlighting the robustness of DNN-based predictions for packing density. It is important to note that two data points in Fig. S8(a) and (d) lie significantly outside the range of the rest of the dataset. These points correspond to linear polymers with N_{bb} =13. They were excluded from the analysis to maintain a coherent training set that accurately reflects the structural characteristics of the grafted polymer class under investigation.

These results confirm that DNN models effectively capture the nonlinear structure-property relationships of graft polymers. The high predictive accuracy for R_g, D, and ρ, along with reasonable agreement for T_g, underscores the potential of deep learning models in polymer informatics. The strong performance of DNNs in predicting ρ further supports the use of image-based representations as an alternative approach to traditional descriptor-based methods in machine learning-driven polymer design.

S3.3 CNN models

We developed CNN models using image representations as input to predict the four properties. Two types of convolutional layers were compared: traditional convolutional layers (CLs) and spatially separable convolutional layers (SCLs). SCLs break down 2D convolutions into simpler 1D operations, reducing computational complexity. Testing revealed CLs as optimal for predicting D and ρ, whereas SCLs were optimal for R_g and T_g. The CNN model was also trained using the same 60:20:20 train-validation-test split, with the same statistical distribution of target properties as shown in Fig. S5.

All CNN models are composed of three convolutional layers with 64, 128, and 256 filters (kernel size: 5×5, padding='same'), each followed by max pooling layers (pool and stride

size: 2×2). A flattening layer connected to dense layers with 256, 512 neurons (ReLU activation), and a single linear output neuron. One example showing the optimization of the learning rate and batch size is in the figure below (Figure S6 (b)). Besides the learning rate and batch size, we also optimized the number of filters, stride size, and pooling.

Filters: The number of filters was systematically varied from 32 to 512 by increasing the filter count in each convolutional layer. The model performed best when the number of filters was doubled progressively from the first to the third layer.

Strides: Both rectangular and square strides were evaluated, with square strides yielding significantly better performance. Among the square strides tested, ranging from (2×2) to (7×7), a stride size of (5×5) produced the best results.

Pooling: Three types of pooling-global pooling, average pooling, and max pooling-were investigated. Max pooling consistently delivered the best predictive performance across all outputs. Regarding pool size and stride, configurations of (1×1), (2×2), and (3×3) were tested, with the (2×2) pool size and stride providing optimal results.

Convergence Behavior

Similar to the DNN models, we also tested the convergence behavior of the CNN models (see Fig. S9). The CNN models exhibit rapid and stable convergence within the first few hundred epochs, with both the training loss (black) and validation loss (red) decreasing consistently. Notably, the validation loss remains consistently below the training loss, indicating strong generalization ability and no signs of overfitting. This consistent convergence across all four predicted properties highlights the robustness of the image-based representation in capturing key structural features of graft polymers.

These loss curves, in conjunction with the high R^2 values reported in the main manuscript, validate that both ML architectures (CNN and DNN) are well-tuned and generalize effectively to unseen data. It is also important to note that the total number of training epochs varies across different models. This is due to the use of early stopping, where training stops if no improvement in validation loss is observed over a set interval. In our case, the interval

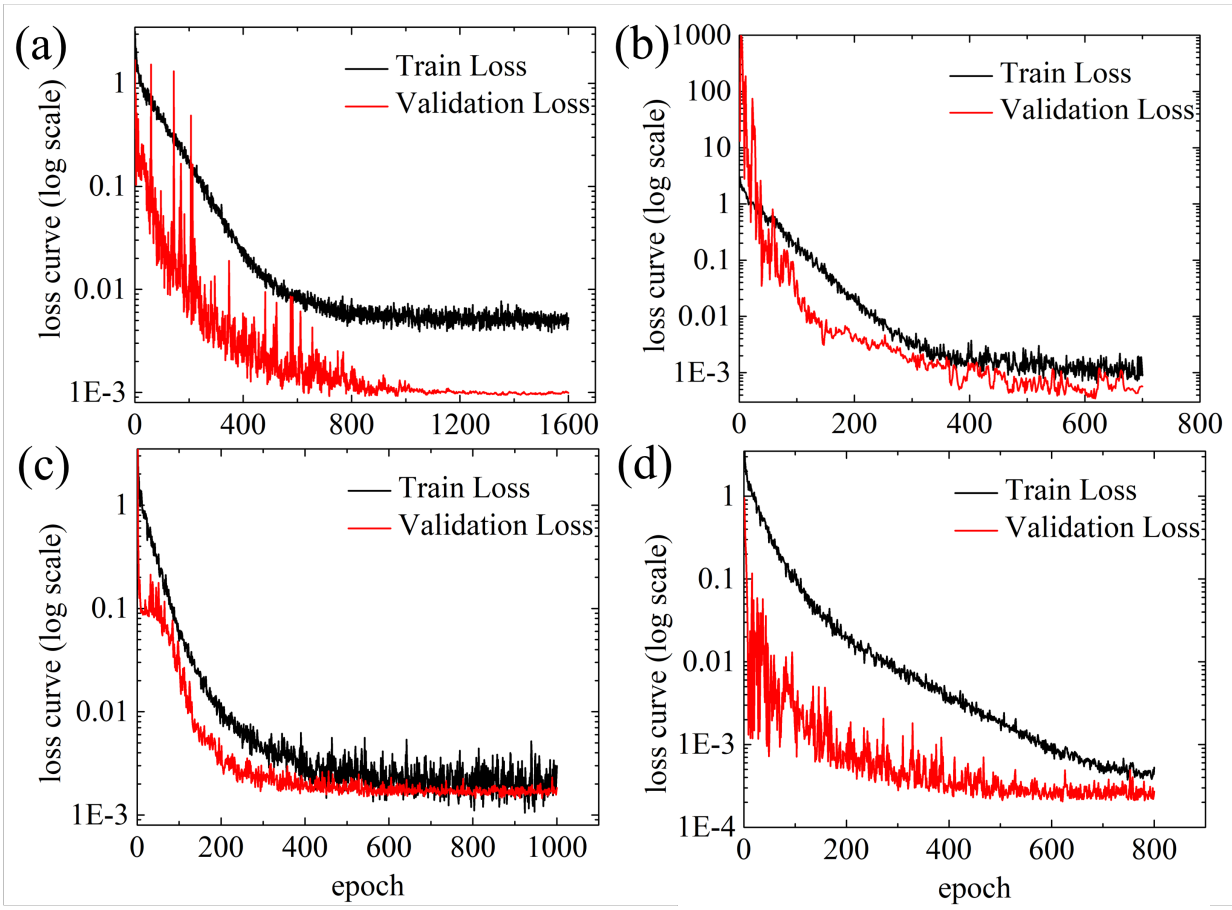

Figure S9: The training and validation loss curves for convolutional neural network models predicting (a) density, ρ (m/σ^{-3}), (b) diffusivity, $D(\sigma^2/\tau)$, (c) radius of gyration, R_g (σ), and (d) glass transition temperature, T_g (ϵ/k_B). The figures show the evolution of loss (in log scale) over training epochs. Black curves represent training loss, and red curves represent validation loss. All models exhibit rapid convergence and stable training behavior, with no signs of significant overfitting. It is to note that the loss values are computed after applying a transformation on output properties, followed by min-max scaling and normalization.

is set to 100 epochs, meaning the model was allowed to continue training until validation loss failed to improve for 100 consecutive epochs. This approach ensures efficient convergence while preventing overfitting.

Prediction Performance of CNN Models

Understanding the prediction accuracy is essential for evaluating the performance of any ML model. Here, we compare the predicted and true values of ρ, R_g, D, and T_g to compute the predictive accuracy of our CNN models trained on black-and-white polymer

representations (see Fig. S8). In this figure, we plotted the comparisons, where the red dashed line represents the ideal scenario where predicted values perfectly match MD simulation results.

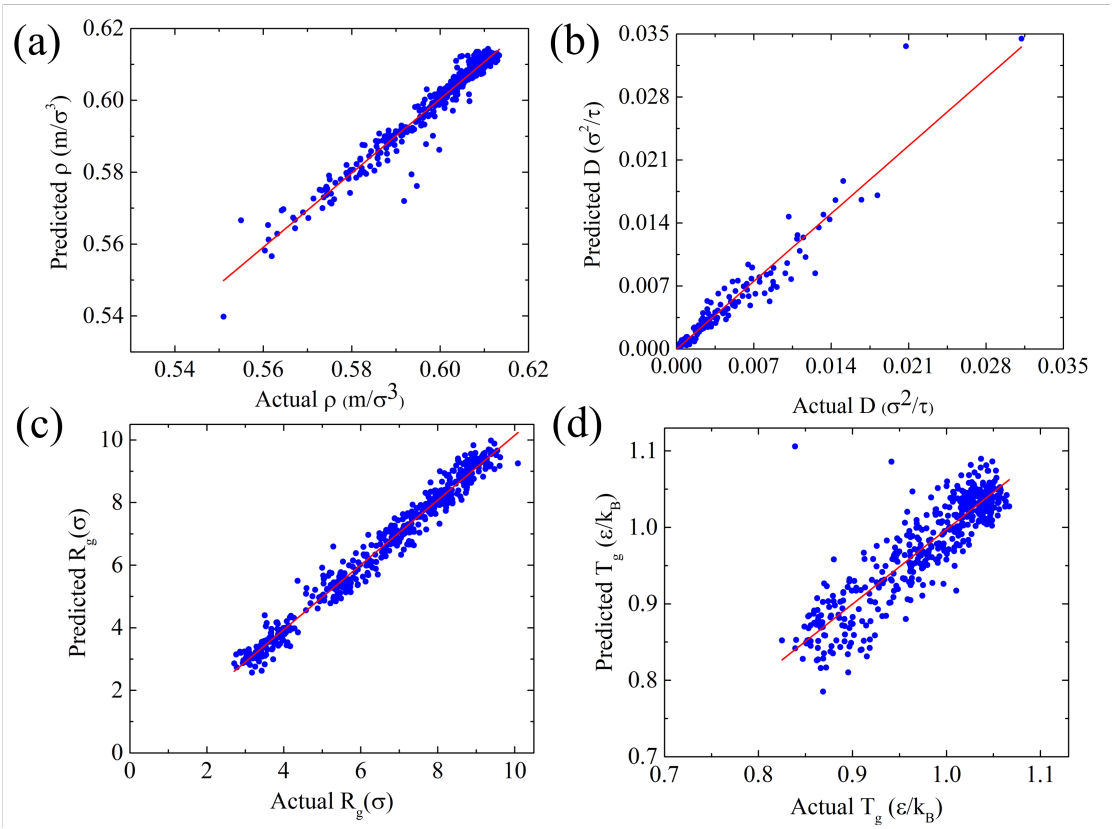

Figure S10: Comparison of predicted and actual values for the four polymer properties using CNN models: (a) density, ρ (m/σ^{-3}), (b) diffusivity, $D(\sigma^2/\tau)$, (c) radius of gyration, R_g (σ), and (d) glass transition temperature, T_g (ϵ/k_B). Each point represents sample data, and the red diagonal line indicates the ideal prediction ($y = x$). The close clustering of data points along the diagonal demonstrates the strong predictive performance of the CNN models.

In Fig. S10(a), we first plotted the prediction for ρ. Here, we can see that the CNN model accurately predicts it, with most data points closely aligned along the diagonal reference line. The predicted values exhibit minimal scatter, indicating strong performance and robustness of the image-based model in capturing packing density. Similarly, the predicted diffusion coefficient D (Fig. SS10(b)) follows the expected trend, although with slightly more variance across the range of values. Despite the increased spread, especially at higher D, the overall alignment suggests that the CNN model effectively captures the key dynamic features

related to polymer mobility. The predictions for R_g (Fig. S10(c)) also demonstrate excellent agreement with actual values across a broad range, further confirming the CNN model's ability to extract conformational information from the image representation. Finally, the glass transition temperature T_g (Fig. S10(d)) is reasonably well-predicted, with points generally distributed around the diagonal, despite some deviations at the higher end. These results collectively confirm that CNN models trained on 2D image representations can achieve high predictive accuracy across diverse polymer properties.

The strong predictive performance for all the physical variables—particularly ρ, R_g, and D—as well as reasonable accuracy for T_g, highlights the utility of such ML models in polymer physics.

S4 Interpreting ML Predictions: Saliency Maps and SHAP Values

To address the interpretability of our machine learning models, we employed saliency mapping and SHAP analysis. These techniques allow us to visualize and quantify the input regions most influential in predicting polymer properties. By analyzing feature attributions, we uncover mechanistic insights that link specific architectural elements to key properties such as T_g, R_g, D, and ρ.

- For T_g, the saliency maps reveal that regions with the highest contributions are clustered around the backbone (rows: 0, columns: 0-30) and the side chains (rows: 1-13). This indicates that backbone beads (row: 0-30) and side-chain beads (1-13) are significant to the T_g prediction. However, T_g is saturated when N_{bb} exceeds 40 regardless of N_{sc} (see Figure 1(c)), consistent with the low-contribution values in the rows 40-60 and columns 5-26 of the saliency map.

- In contrast, the saliency map for R_g shows high-contribution regions at both the top

and bottom across almost all columns. This pattern suggests that the terminal regions of long side chains and the backbone are key drivers of high R_g, consistent with intuitive and theoretical expectations for polymer size scaling.

- For D and ρ, the saliency maps consistently highlight the backbone as the most influential factor, underscoring its role in determining steric hindrance and free volume within the polymer structure.

To further interpret the DNN models trained on physical descriptors, we computed the mean absolute SHAP values for each of the six input features across the four predicted properties (T_g, R_g, D, and ρ). The results shown in Figure S11 indicate that the average side-chain length ($N_{sc,ave}$) has the most significant impact on the DNN model for predicting T_g highlighting the role of side chains in the thermodynamic properties of graft polymers. In predicting R_g, the top two important descriptors are N_{bb} and N_{tot}, suggesting that backbone and overall degree of polymerization governs the size of the graft polymer. For diffusivity (D) and packing density (ρ), N_{bb} is the most important feature. These insights demonstrate how specific architectural features govern different physical properties and enhance interpretability of the learned structure–property relationships.

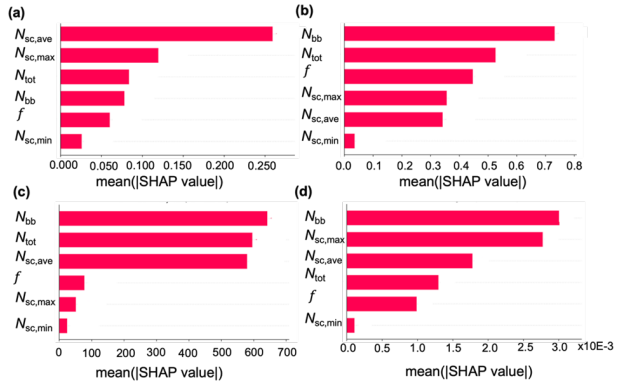

Figure S11: The summary of the mean |SHAP value| of all the 6 physical descriptors for predicting (a) T_g, (b) R_g, (c) D, and (d) ρ by the DNN models.

Finally, to evaluate the interpretability of DNN models trained on graphical descriptors, we computed the mean absolute SHAP values for all 11 input features across the predicted

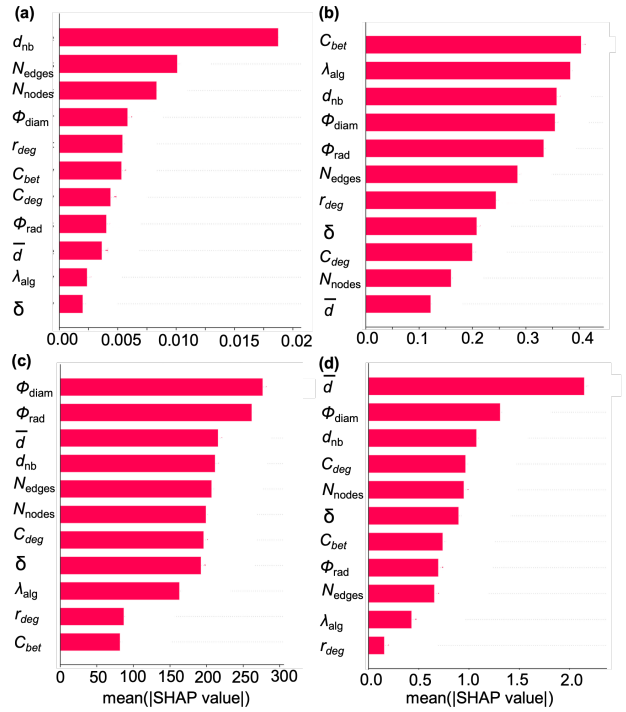

Figure S12: The summary of the mean |SHAP value| of all the 11 graphical descriptors for predicting (a) T_g, (b) R_g, (c) D, and (d) ρ by the DNN models.

properties (T_g, R_g, D, and ρ). As shown in Figure S12, the average neighbor degree ($\bar{d}_{nb}$) ranks the highest, highlighting the importance of more branches and long backbone and side-chain length. In the case of R_g, the mean betweenness centrality (C_{bet}) is the most influential feature, reflecting the spatial distribution of polymer segments. The diffusion coefficient D and packing density ρ are similarly affected by global topological measures such as diameter (ϕ_{diam}) and average degree ($\bar{d}$), emphasizing how global size/shapes influence dynamic and thermodynamic behavior. Compared to physical descriptors, graphical features offer a more nuanced representation of architectural variation, which aids in capturing complex structure-property relationships.

S5 General Design Rules for Material Discovery

This section summarizes how the observed structure-property relationships can guide polymer design and how the developed framework accelerates material discovery. Based on the

systematic dataset of graft and bottlebrush polymers, and supported by model interpretability tools (Shapley values and saliency maps), we identify the following general design principles that govern the physical and dynamic properties of these systems:

- **Side-chain positioning**: The spatial location of side chains along the backbone critically affects both polymer conformation and dynamics. When side chains are positioned near the termini of the backbone—particularly at low grafting density—the polymer adopts a more extended configuration, resulting in a higher radius of gyration (R_g) and a reduced diffusion coefficient (D) due to increased segmental crowding. Conversely, central placement of side chains at high grafting density leads to more compact structures with lower R_g. Importantly, the glass transition temperature (T_g) is only weakly influenced by side-chain positioning and shows stronger dependence on backbone length. These observations indicate that D and T_g can be modulated independently through architectural design.

- **Backbone and side-chain length:** The backbone length and the maximum side-chain length ($N_{\mathrm{sc,max}}$) exert a strong influence on all four target properties (T_g, R_g, D, and ρ), whereas the minimum side-chain length ($N_{\mathrm{sc,min}}$) contributes negligibly. This conclusion is supported by both the low Shapley value of $N_{\mathrm{sc,min}}$ in the DNN model and its weak Spearman correlation with the predicted properties. These findings suggest that topological features such as backbone length and $N_{\mathrm{sc,max}}$ serve as effective and interpretable design parameters for tuning the thermal, structural, and dynamic behavior of graft polymer systems.

These design guidelines offer a rational strategy to optimize both thermal and dynamic properties of graft polymers.

References

(1) Karuth, A.; Alesadi, A.; Xia, W.; Rasulev, B. Predicting glass transition of amorphous polymers by application of cheminformatics and molecular dynamics simulations. *Polymer* **2021**, *218*, 123495.

(2) Chremos, A.; Jeong, C.; Douglas, J. F. Influence of polymer architectures on diffusion in unentangled polymer melts. *Soft Matter* **2017**, *13*, 5778–5784.

(3) Thompson, A. P.; Aktulga, H. M.; Berger, R.; Bolintineanu, D. S.; Brown, W. M.; Crozier, P. S.; in 't Veld, P. J.; Kohlmeyer, A.; Moore, S. G.; Nguyen, T. D.; Shan, R.; Stevens, M. J.; Tranchida, J.; Trott, C.; Plimpton, S. J. LAMMPS - a flexible simulation tool for particle-based materials modeling at the atomic, meso, and continuum scales. *Comput. Phys. Commun.* **2022**, *271*, 108171.

(4) Frenkel, D.; Smit, B. *Understanding Molecular Simulation : From Algorithms to Applications, 2nd Ed.*; Academic Press, 2002.

(5) Frenkel, D.; Smit, B. *Understanding Molecular Simulation (Second Edition)*, second edition ed.; Academic Press: San Diego, 2002; pp 139–163.

(6) Xu, X.; Douglas, J. F.; Xu, W.-S. Influence of Side-Chain Length and Relative Rigidities of Backbone and Side Chains on Glass Formation of Branched Polymers. *Macromolecules* **2021**, *54*, 6327–6341.

(7) Xu, W.-S.; Douglas, J. F.; Freed, K. F. Generalized entropy theory of glass-formation in fully flexible polymer melts. *The Journal of Chemical Physics* **2016**, *145*, 234509.

(8) Xu, X.; Douglas, J. F.; Xu, W.-S. Generalized entropy theory investigation of the relatively high segmental fragility of many glass-forming polymers. *Soft Matter* **2025**, *21*, 2664–2685.

(9) Jiang, S.; Dieng, A. B.; Webb, M. A. Property-guided generation of complex polymer topologies using variational autoencoders. *npj Computational Materials* **2024**, *10*, 139.